

# Micropulsion Using a Laser Ablation Jet

C. Phipps\*

Photonic Associates, Santa Fe, New Mexico 87508

J. Luke†

New Mexico Institute of Mining and Technology, Institute for Engineering Research and Applications,  
Albuquerque, New Mexico 87106-4339

and

T. Lippert,‡ M. Hauer,§ and A. Wokaun¶

Paul Scherrer Institut, CH-5232 Villigen PSI, Switzerland

We investigated exothermic laser ablation “fuels” for the micro Laser Plasma Thruster ( $\mu$ LPT), a novel type of microthruster. Using ms-duration laser pulses, which are required for multi-mode laser diodes to exceed ablation threshold fluence in the smallest focal spots available with conventional optics, successful target materials were restricted to those of low thermal conductivity, i.e., polymers, not metals. Polymers studied included carbon-doped polyvinylchloride for a passive target baseline, and several carbon-doped exothermic photopolymers specifically designed for their task, including polyvinylalcohol, a triazene polymer and a proprietary exothermic polymer (EP). In our single-shot impulse test setup, millimetric fuel samples were evaluated using a tiny torsion pendulum. Promising polymers were then made into fuel tapes and tested for continuous thrust under repetitive-pulse excitation. Two-layer fuel tapes consisted of a transparent supporting layer through which the light passed to ignite an absorbing fuel layer which formed a jet on the opposite side of the tape from that illuminated by the laser, an example of confined ablation. Best results were obtained with EP-1 up to 680  $\mu$ N thrust with 2.1 W average optical power incident and jet velocity of 2–3 km/s. Repeatability of our thrust-measuring torsion pendulum was improved to 1  $\mu$ N.

## Introduction:

### Micropulsion and the $\mu$ Laser Plasma Thruster

THE micro laser plasma thruster ( $\mu$ LPT) (Fig. 1) is a novel, subkilogram micropulsion module for attitude control and propulsion of sub-100-kg satellites.<sup>1</sup> Potential applications range from controlling the attitude and relative position of elements in a constellation of micro- and nanosatellites to achieving high positional accuracy in long-baseline space-based interferometer missions such as LISA.<sup>2</sup>

For a 25-kg-mass microsatellite, the most important criterion for an attitude- or position-control thruster is small mass because 6–12 single-axis thrust units are required to provide position and rotation control. Electric propulsion is highly desirable for thrust control and to avoid toxic and hazardous chemicals and reaction products. Desirable operating parameters are 75- $\mu$ N thrust and 300-N·s lifetime impulse.

Mueller,<sup>3</sup> Mueller et al.,<sup>4</sup> and Phipps and Luke<sup>5</sup> have provided excellent summaries of current alternatives for micropulsion. Several of these have been under development for 20–30 years. Each has attractive features, as well as problematic limitations. A review of the state of the art shows that a radically new approach might be beneficial.

The  $\mu$ LPT is just such a new departure in electric micropulsion and will be the first application of laser ablation to space propul-

sion. It takes advantage of the predictable physics of laser–materials interaction. Power density on target is optically variable in an instant, and so exhaust velocity can be adjusted during flight to match optimum values. The  $\mu$ LPT requires no neutralizers, heaters, high-voltage supply, high-voltage switches, magnetic fields, nozzle, gas tanks, or valves. It is also free of mysterious small-scale physics.

Most importantly for the technology as a whole, nothing erodes during operation except the ablation fuel. The source of concentrated power is physically separate from the thrust-generation chamber, so that only the fuel ablates, not the engine itself.

Its output is a narrow laser-generated plasma jet with a width with visual luminosity about 25-deg full width at half maximum (FWHM). Thus far, the only quantitative measurements of the plume distribution that we have made were of the carbon deposited by the jet on a witness plate. This subtends a larger solid angle (about 40 × 60 deg FWHM). Direct simulation Monte Carlo (DSMC)/particle-in-cell (PIC) simulations of the jet leaving a planar surface have given good agreement with the carbon plume data.<sup>6</sup>

Several other  $\mu$ LPT fuel types and configurations have been reported.<sup>7–12</sup> See Table 1 for a list of symbols and their definitions.

## Goals of this Work

The problem we addressed in this work was to try to improve the performance parameters we obtained from polyvinylchloride (PVC) in earlier work<sup>1</sup> by the use of exothermic target materials. The most important of these were ablation efficiency (proportional to the product of laser momentum coupling coefficient  $C_m$  and specific impulse  $I_{sp}$ ). We also hoped that the laser energy required to initiate the jet could be reduced with exothermic materials to obtain equal performance with less laser power.

These problems are peculiar to the use of laser diodes to illuminate ablation targets to produce thrust, the technology that is the basis of our current  $\mu$ LPT. Laser diodes are essentially constant optical power devices. For this reason, even with quite small focal spots, pulse durations as long as 1 ms are necessary to deliver enough fluence to exceed the plasma threshold (Fig. 2, Ref. 1). Further, at these long pulse durations, we found that only materials with low thermal conductivity, that is, some polymers but no metals, were

Received 31 May 2003; revision received 30 December 2003; accepted for publication 25 February 2004. Copyright © 2004 by Photonic Associates. Published by the American Institute of Aeronautics and Astronautics, Inc., with permission. Copies of this paper may be made for personal or internal use, on condition that the copier pay the \$10.00 per-copy fee to the Copyright Clearance Center, Inc., 222 Rosewood Drive, Danvers, MA 01923; include the code 0748-4658/04 \$10.00 in correspondence with the CCC.

\*President, 200A Ojo de la Vaca Road; crphipps@aol.com. Member AIAA.

†Senior Research Engineer, 901 University Boulevard Southeast.

‡Head, Materials Group.

§Ph.D. Student, Materials Group.

¶Head, General Energy Research Department; also Professor, Chemistry Department, ETH Zurich.

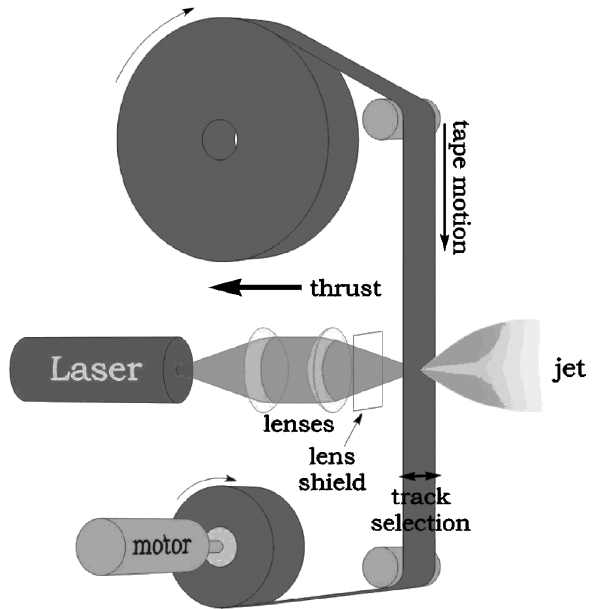
**Table 1** Symbols used in this paper

| Symbol          | Meaning  | Units           |
|-----------------|--|-----------------|
| $A$             | Atomic mass  | amu             |
| $A_{ab}$        | Interaction area on target $\gg \pi d_s^2/4$           | $m^2$           |
| $A_s$           | Laser spot area on target                              | $m^2$           |
| $C_m$           | Laser momentum coupling coefficient                    | N/W             |
| $C_v$           | Specific heat at constant volume                       | J/(kg · K)      |
| $D$             | Diameter of fuel tape holes                            | m               |
| $d$             | Spacing between fuel tape holes, or $(d_x d_y)^{0.5}$  | m               |
| $d_s$           | Incident laser beam diameter (FWHM)                    | m               |
| $d_x, d_y$      | Orthogonal measurements of hole size in VIFT technique | —               |
| $E$             | Shorthand for $10^6$                                   | —               |
| $g$             | Acceleration of gravity                                | $m/s^2$         |
| $h_c$           | Specific internal chemical energy                      | J/kg            |
| $h_{Et}$        | Specific vapor kinetic energy at ignition threshold    | J/kg            |
| $h_f$           | Specific heat of fusion                                | J/kg            |
| $h_v$           | Specific heat of vaporization                          | J/kg            |
| $I$             | Incident laser intensity                               | $W/m^2$         |
| $I_{sp}$        | Specific impulse                                       | s               |
| $I_{ssp}$       | System specific impulse                                | s               |
| $k$             | Dry mass to expendable fuel mass ratio                 | —               |
| $M$             | Total mass of ablation fuel                            | kg              |
| $M^2$           | Beam quality factor                                    | —               |
| $m$             | Mass ablation rate                                     | $kg/s$          |
| $m_p$           | Proton mass  | kg              |
| $N_A$           | Avogadro number  | —               |
| $Q^*$           | Specific ablation energy                               | J/kg            |
| $q_v$           | Energy density for ablation                            | $J/m^3$         |
| $v_E$           | Exhaust velocity                                       | m/s             |
| $v_{Et}$        | Exhaust velocity at ignition threshold                 | m/s             |
| $t$             | Total thickness of the material propelled by ablation  | m               |
| $T$             | Optical transmission of transparent layer              | —               |
| $T_0$           | Initial temperature                                    | K               |
| $T_v$           | Vaporization temperature                               | K               |
| $W$             | Incident laser pulse energy                            | J               |
| $w_0$           | Beam waist diameter at best focus, $z = z_0$           | m               |
| $w(z)$          | Beam waist diameter at $z$                             | m               |
| $x_v$           | Thickness of ablated material, $\leq t$                | m               |
| $x_T$           | Thermal penetration depth                              | m               |
| $z$             | Axial coordinate parallel to beam propagation          | m               |
| $z_0$           | Value of $z$ at best focus                             | m               |
| $\alpha$        | Absorption coefficient in the ablating material        | $m^{-1}$        |
| $\Delta m$      | Mass loss in a single shot with the impulse test stand | —               |
| $\eta_{ab}$     | Ablation efficiency                                    | —               |
| $\Phi$          | Incident laser fluence, $W/(\pi d_s^2/4)$              | $J/m^2$         |
| $\Phi_{ab}$     | Ablation fluence, $W/A_{ab}$                           | $J/m^2$         |
| $\Phi_{coh}$    | Fluence required to overcome material cohesion         | —               |
| $\Phi_t$        | Ablation fluence below detonation threshold            | $J/m^2$         |
| $\Phi'_t$       | Ablation fluence just above detonation threshold       | $J/m^2$         |
| $\lambda_{eff}$ | $M^2\lambda$ , effective wavelength                    | m               |
| $\mu$           | Mass areal density                                     | $kg/m^2$        |
| $\sigma$        | Momentum areal density                                 | $N \cdot s/m^2$ |
| $\rho$          | Target mass density                                    | $kg/m^3$        |
| $\tau$          | Laser pulselwidth                                      | s               |
| $\xi$           | $\Phi_{ab}/\Phi_t$                                     | —               |

suitable targets because thermal diffusion in the target during the pulse otherwise prevented plasma formation.<sup>1</sup>

We deliberately designed photopolymers that would have a good chance of accomplishing our goals. Using the performance of the best passive, that is, nonexothermic, polymers as a baseline, we report the performance of these new polymers. One of them was sufficiently successful that its precise composition is proprietary, and it will be referred to simply as exothermic polymer (EP-1). The other two are polyvinyl alcohol and a triazene polymer.

In what follows, we will summarize the physics of the laser-material interaction in the fuel tape geometry that we use. Then, we will discuss polymer design and the construction of the tapes; the design and operation of the testbed  $\mu$ LPT; the two test setups and associated measurement errors; and, last, the results of our work and conclusions from it.

**Fig. 1** Schematic of the  $\mu$ LPT.

## Laser–Material Interaction

### Basic Concepts

For the sake of simplicity, we will consider a monoenergetic exhaust stream with velocity  $v_E$ . We have shown<sup>13,14</sup> that this approximation will not introduce large errors [ $\langle v^2 \rangle / \langle v \rangle^2 \approx 1.15$ ] for typical laser-produced plasma jets, and the principal points we want to make here will be made more transparently by the use of that assumption.

In the ablation process,  $Q^*$  J of laser light are consumed to ablate unit mass of target material, and  $C_m$  units of impulse are produced. The product of  $C_m$  and  $Q^*$  is, in fact, the exhaust velocity  $v_E$  of the ablation stream, given the monoenergetic assumption. This can be seen by combining the definitions of  $C_m$  and  $Q^*$ :

$$C_m Q^* = (\Delta m v_E / W)(W / \Delta m) = v_E \quad (1)$$

independent of the ablation efficiency  $\eta_{ab}$ . If, for example, a significant amount of the incident energy is absorbed as heat in the target substrate rather than producing material ejection,  $Q^*$  will be higher and  $C_m$  will be proportionately lower, giving the same velocity in the end. In propulsion work, specific impulse  $I_{sp}$  is customary notation for  $v_E/g_0$ . In this work, we define  $I_{sp}$  as

$$I_{sp} = C_m Q^* / g \quad (2)$$

Energy conservation prevents  $C_m$  and  $I_{sp}$  from being arbitrary. An increase in one decreases the other. Energy conservation requires that several constant product relationships exist:

$$2\eta_{ab} = \Delta m v_E^2 / W = C_m^2 Q^* = g_0 C_m I_{sp} = C_m v_E \quad (3)$$

In Eq. (3), we introduce the ablation efficiency parameter,  $\eta_{ab} \leq 1$ , the ratio of exhaust kinetic energy to incident laser energy  $W$ . This definition means that  $\eta_{ab}$  can actually be  $> 1$  for exothermic targets.

For passive targets,  $\eta_{ab} \leq 1$ , and the product

$$C_m I_{sp} \leq 2/g_0 = 0.204 \quad (4)$$

The maximum specific impulse of ordinary chemical rockets is about 500 s, limited by the temperatures available in chemical reactions. For example, the heat of formation for hydrogen–oxygen combustion, one of the hottest chemical reactions, is 57.8 kcal/mole (Ref. 15). This translates to a reaction temperature of  $2.91E4K$ , for which the most probable thermal velocity  $(2 kT/m_E)^{0.5} = 5.17 \text{ km/s}$ , or  $I_{sp} = 527 \text{ s}$ . However, for example, the space shuttle's main engine can produce only 465 s ( $v_E = 4.56 \text{ km/s}$ ), because of inefficiencies inherent in the engine.<sup>16</sup>

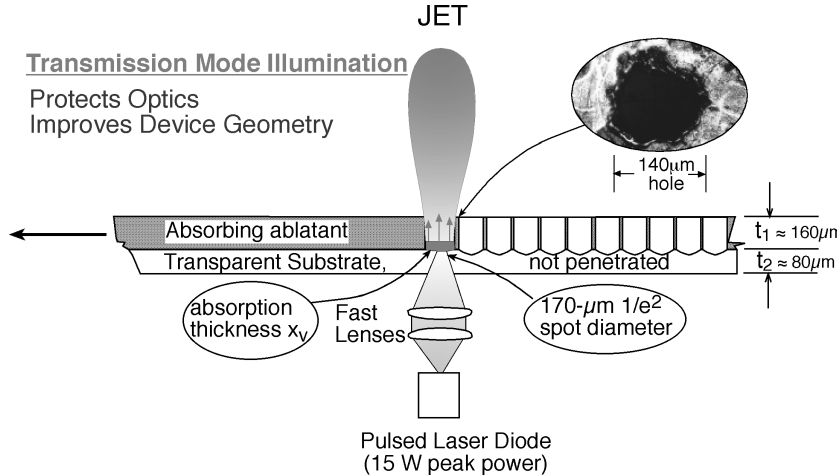


**Fig. 2 Target illumination geometry.** Illumination in so-called “Transmission Mode” illumination guarantees the conditions of “volume absorption” in our theoretical model. The laser is operated repetitively pulsed, with pulse duration (1 ms) much less than the time for the hole created to move across the laser focus (7 ms). Each pulse passes through the transparent substrate and creates a detonation at the interface between it and a carbon-doped ablative layer. The detonation expands to produce the jet. The transparent substrate is not penetrated, although some of it may also ablate. Typically, 70% of the material in the hole is utilized. However, to avoid plume steering, the holes with diameter  $D = 140 \mu\text{m}$  must be separated by a  $d = 20\text{-}\mu\text{m}$  rim of material, giving an overall mass-utilization efficiency for the entire tape of  $0.7^*\pi/4^*[D/(D+d)]^2$ , or about 40%.

This limit is fundamental, and will not change with improvements in engine materials. Larger  $I_{\text{sp}}$  values (exit velocity  $v_E \gg 5 \text{ km/s}$ ) are accessible only by laser ablation, where temperatures can be more than  $1E6\text{K}$  for nanosecond duration pulses, or some other nonchemical process such as ion drives. Specific impulse  $I_{\text{sp}}$  up to 7600 s has been measured<sup>14</sup> with lasers with 20-ns-duration pulses from an ordinary KrF laser illuminating Al. This  $I_{\text{sp}}$  corresponds to  $T = 9.1E6 \text{ K}$  (780 eV).

Ablation efficiency can approach 100%, as direct measurements with other types of lasers on cellulose nitrate in vacuum verify, but a value of 50%, or even less, is likely<sup>14</sup> unless strict attention is paid to the illumination geometry.

$I_{\text{sp}}$  and so-called “system specific impulse”  $I_{\text{ssp}}$ , are related by<sup>17</sup>

$$I_{\text{ssp}} = I_{\text{sp}}(1 + k) \quad (5)$$

where

$$k = M_{\text{dry}}/M_{\text{fuel}} \quad (6)$$

The corresponding “system coupling coefficient”  $C_{\text{ms}}$  is just the thrust to electrical power input ratio of the entire system.

#### Optimizing $C_m$ and $I_{\text{sp}}$

When  $C_m$  and  $Q^*$  are considered as design variables, it must be kept in mind that large  $C_m$  is not always useful. The ablator lifetime increases with  $Q^*$  and decreases very rapidly with increasing  $C_m$  (Ref. 15):

$$\tau_{\text{ab}} = \left| \frac{M}{\dot{m}} \right| = \frac{MQ^*}{P} = \frac{2E7\eta_{\text{ab}}M}{PC_m^2} = \frac{g^2MI_{\text{sp}}^2}{2E7P\eta_{\text{ab}}} \quad (7)$$

In vacuum, ignoring gravity, the energy cost  $C$  is given by the expression<sup>11</sup>

$$C = (v_E^2/2E7)[\exp(\Delta v/v_E) - 1] \quad (8)$$

for which the optimum (minimum) cost is given by<sup>18</sup>

$$\Delta v/v_E = 1.5936 \quad (9)$$

Large  $C_m$  and low  $I_{\text{sp}}$  is a good trade only for short-duration missions. When  $C_m$  is unduly high, a lot of thrust is generated per unit of laser power, but the low  $I_{\text{sp}}$  means that the fuel is depleted before the mission can be completed. [See Eq. (7).] In contrast an

engine with unduly high  $I_{\text{sp}}$  preserves the fuel indefinitely, but has no thrust.

Because we are interested in maximum operating lifetime  $\tau_{\text{ab}}$ , in this work our goal is to obtain the maximum value of  $I_{\text{sp}}$  consistent with the plasma temperatures that can be produced by a millisecond-duration diode, approximately 1000 s. If  $\eta_{\text{ab}} = 1$  were possible (and it can be with exothermic targets), the corresponding values of the other variables would be  $C_m = 204 \mu\text{N/W}$ ,  $v_E = 9.8 \text{ km/s}$ , and  $\Delta v = 15.6 \text{ km/s}$ .

We note that the purposes of using laser-initiated exothermic targets, rather than just using an exothermic fuel as a rocket without the laser, are the control of ignition, including proportional response with repetitively pulsed engines, and the higher temperatures achievable with laser-driven chemistry than with chemistry by itself.

#### Plasma Formation Threshold

An important consideration in the optimization of laser-plasma generated thrust is the definition of the laser intensity required for maximizing  $C_m$ . This is accomplished by operation at laser intensity close to the vapor-plasma transition because, on both sides of this maximum,  $C_m$  decreases, both below by decreasing  $v_E$  in the vapor phase, and above by plasma shielding of the target. This optimum intensity, which is essentially identical to the plasma threshold, is given by<sup>1</sup>

$$I_{\text{opt}} = 240/\tau^{0.55} \quad (10)$$

in megawatts per square meter. Equation (10) is a useful guide valid to within factors of two for millisecond to sub-nanosecond pulse durations for all surface absorbing materials in vacuum and for visible to infrared wavelengths. It is also a useful guide for the prediction of plasma initiation in confined ablation.

#### Laser Momentum Coupling Literature

The vacuum laser momentum coupling literature consists of cases that may be described as 1) surface absorption, 2) volume absorption, and 3) confined ablation. Targets, in turn, may be identified as passive (nonexothermic) or exothermic. In case 1, laser energy is absorbed at the surface, rather than within the depth of the target, and the absorption is often mediated by a plasma absorption layer.<sup>19</sup> Cases 2 and 3 are similar to each other, in that laser absorption occurs not at the surface, but deep within the material, which is homogeneous in case 2 and heterogeneous in case 3.

Table 2 lists the laser momentum coupling literature, beginning in the top row with typical passive front-illuminated materials and

**Table 2** Summary of large laser momentum coupling measurements in the literature

| Reference | Target  | Laser<br>$\lambda, \tau$          | Minimum laser<br>$\Phi, \text{J/m}^2$ | Maximum<br>$C_m, \mu\text{N/W}$ | Maximum $I_{sp}, \text{s}$<br>[or, upper bound from Eq. (3)] |
|-----------|---|-----------------------------------|---------------------------------------|---------------------------------|--|
| 18        | Passive front illuminated                         | Various                           | Various                               | 100                             | —  |
| 13        | Pyroxylin exothermic (volume ablation)            | 10.6 $\mu\text{m}, 2 \mu\text{s}$ | 5E10                                  | 950                             | 200  |
| This work | Proprietary exothermic absorber (volume ablation) | 970 nm, 2 ms                      | 2E7                                   | 520                             | 550  |
| 33        | Confined passive absorber                         | 1.06 $\mu\text{m}, 85 \text{ ns}$ | 1E4                                   | 4920                            | 1.0  |
| 20        | Confined passive absorber                         | 1.06 $\mu\text{m}, 3 \text{ ns}$  | 2E3                                   | 7000                            | [≤29]  |
| 34        | Confined passive absorber (simulation)            | 1.06 $\mu\text{m}, 50 \text{ ns}$ | 1E3                                   | 60,000                          | [≤3.4]   |

progressing to those for confined ablation of exothermic materials. Equation (4) forces exhaust velocity to be only a few meters per second for the largest  $C_m$  values in Table 2, and such low  $v_E$  values are cost efficient for  $\Delta v$  of similar magnitude.

The main point of Table 2 is that  $C_m$  values as large as 7000  $\mu\text{N/W}$  have been observed with confined ablation, even of passive materials, whereas standard surface absorbers rarely exceed 100  $\mu\text{N/W}$ .

### Confined Ablation Model

A close cousin of confined ablation is volume absorption, for which a theory was originally developed<sup>19</sup> to describe the situation in which a homogeneous target with laser absorption depth  $1/\alpha$ , much larger than the thermal penetration depth  $x_T = (\kappa\tau)^{1/2}$ , absorbs most of the incident laser energy below, rather than on, the surface. Sufficient laser-pulse fluence can then vaporize and drive off a chunk of target material from beneath, producing more momentum for the same laser energy investment. During the process, pressure builds up beneath the surface, due to the inertia of the outer layers of material (a phenomenon known in explosives work as “tamping”). Pressure enhancement due to tamping can be an order of magnitude, or more.

Figures 1 and 2 show the concept of the microthruster and the geometry of target illumination in our work. The specially prepared, two-layer fuel tapes consist of a transparent supporting layer through which the laser light passes to ignite an absorbing fuel layer which forms a jet on the opposite side of the tape from that illuminated by the laser. Ignition initiates at the interface between the two materials, so this arrangement is an example of the confined ablation geometry.<sup>20</sup>

The theory for confined ablation originally developed by Fabbro et al.<sup>21</sup> does not work well for long pulses of order 1 ms because the expression for  $C_m$  has only one term that varies as  $I^{-0.75}$  and “blows up” at low intensity. Instead, we have adapted our original theory for this situation<sup>20</sup> to apply to the Fig. 2 confined ablation geometry.

We begin with the Srinivasan et al. definition of  $x_v$ , the ablation depth (less than or equal to the ablation layer thickness  $t$ )<sup>20</sup>

$$x_v = l_n(\Phi/\Phi_t)/\alpha = l_n\xi/\alpha \quad (11)$$

In Eq. (11),  $\Phi_t$  is the fluence required to just begin decomposition of the absorbing target polymer and can be written as<sup>22,23</sup>

$$\Phi'_t = (\rho/\alpha)[h_{Et} + h_f + h_v + C_v(T_v - T_0) - h_c] \quad (12a)$$

just above threshold, and

$$\Phi_t = (\rho/\alpha)[h_f + h_v + C_v(T_v - T_0)] \quad (12b)$$

just below threshold for decomposition of the exothermic photopolymer, and  $\alpha\Phi_t$  is an energy density (Joules per cubic meter). In Eqs. (12), the quantity  $h_{Et}$  is the kinetic energy of the accelerated vapor just above the threshold expressed in Joules per kilogram:

$$h_{Et} = N_A m_p v_{Et}^2 / 2 \quad (13)$$

Because the common parameters do not change over the infinitesimal change in conditions between Eqs. (12a) and (12b), the new parameters must balance, and

$$h_c = h_{Et} \quad (14)$$

to the level of approximation in which we are interested. In Eq. (13),  $N_A$  is Avogadro’s number,  $m_p$  is the proton mass, and  $v_E$  is exhaust velocity of the (assumed monatomic, monoenergetic) exhaust stream formed by the chemical energy release at the detonation threshold, which is taken to be synchronous with the ablation threshold. Note that no ionization component is necessarily present in Eq. (12a): The threshold concerns, by definition, the onset of vaporization, which precedes plasma formation. At fluences well above threshold, plasma is certainly formed.

The exhaust velocity  $v_E$  at the threshold predicted by Eq. (13) by the use of measured values of  $h_c$  will be compared later with values of  $v_E$  obtained at higher fluences from the product  $C_m Q^*$ . Then, because

$$\mu = \rho t \quad (15)$$

$$C_m = \sigma/\Phi_{ab} \quad (16)$$

The laser fluence available at the interface between the transparent and absorbing media is  $\Phi_{ab}T$ .

Even though the threshold for ablation is exceeded, the internal pressure generated by laser illumination will not be sufficient to overcome material cohesion and produce a jet until an additional fluence  $\Phi_{coh}$  is provided. Accordingly, we write

$$\sigma^2/2\mu = \Phi_{ab}T - \Phi_{coh} - \alpha x_v \Phi'_t \quad (17)$$

where  $\Phi_{coh}$  is the fluence required to overcome the target material cohesion.

There results

$$C_m^2 = (2\rho t/\Phi_{ab})(T - \Phi_{coh}/\Phi_{ab} - l_n\xi/\xi) \quad (18)$$

We evaluate Eq. (18) numerically, requiring that  $(T - \Phi_{coh}/\Phi_{ab} - l_n\xi/\xi) \geq 0$  and requiring that, if  $x_v \geq t$ , then  $l_n\xi = \alpha t$  and if  $x_v \leq x_{v\min}$ , then  $l_n\xi = \alpha X_{v\min}$ , where we arbitrarily set  $x_{v\min} = 10 \mu\text{m}$ . The parameters  $\Phi_{coh}$  and  $\Phi'_t$  are taken as adjustable parameters to best fit experimental data, rather than being calculated from first principles because these parameters are not yet known for our target materials.

### Propagating Detonation

Whether or not a shock is formed is an important consideration when the illumination of an exothermic target material is planned to determine whether a laser-initiated detonation can propagate in an uncontrolled fashion and to predict in all targets whether spallation will occur.

The classic analysis of high-intensity laser interaction with materials divides into two regimes: laser-supported combustion (LSC) and laser-supported detonation (LSD).<sup>24–26</sup> Although the analysis was originally developed by aerodynamicists for interactions in air, these concepts can also apply to a solid target in vacuum. The transition from the LSC to LSD regime is caused by laser intensity sufficient to produce a shock wave in the material, that is, wave velocity greater than the particle thermal velocity.

For our purposes, it is sufficiently accurate to describe shock formation by the relationship

$$\nabla p = \rho v \cdot \nabla v \quad (19)$$

from which

$$p = \rho v^2 = \rho c_s^2 \quad (20)$$

Taking sound speed  $c_s = 1$  km/s and mass density  $\rho = 1000$  kg/m<sup>3</sup>, we find laser-induced pressure  $p \cong 1E9$  N/m<sup>2</sup> = 10 kbar is necessary to produce a shock. The energy density involved is

$$u = \frac{3}{2}nkT = \frac{3}{2}p = \frac{3}{2}(1E9) \quad (21)$$

Joules per cubic meter. In practical terms, the required deposited energy  $u = 1.5E9$  J/m<sup>3</sup>. The laser-induced pressure is  $p = C_m I$ . The maximum intensity we employ, 660 MW/m<sup>2</sup>, and the maximum  $C_m$  we observed (640  $\mu$ N/W) combine to give a pressure  $4.22E5$  N/m<sup>2</sup>, far below the value required to produce a shock.

Moreover, we observed that, the actual interaction area  $A_{ab}$  is, on average, 3 times larger than the laser spot size on target, and, therefore, the true maximum pressure generated is 0.5 bar, and about 0.005% of the value required to initiate a propagating detonation.

Additionally, the thin, planar configuration of our tape targets leads to rapid attenuation of a point-source pressure wave in the target plane, whereas propagation is prohibited in the direction normal to the plane.

### Microthruster Description

Figure 3 shows the testbed  $\mu$ LPT. Table 2 lists the performance parameters for the testbed. Four repetitively-pulsed, fiber-coupled JDSU type 6380-A/L2 laser diodes drive the ablation of the fuel tape. These are capable of 2.5 W output CW at 910–920 nm wavelength with input current and voltage of 3.37 A and 1.71 V, giving 43% electrical efficiency at this output level. At 1 ms pulse duration, we determined that these could achieve peak delivered power output of 3.75 W at 10% duty cycle without damage. The ends of the four 100- $\mu$ m-core-diameter fibers were stripped of their buffer layer for closest spacing, and mounted in a fiber vise. Their light output was collimated with a Lightpath, Inc. GPX5-5 graded axial index aspheric lens and focused with a Thorlabs C330-TM-B aspheric. The EFL's of the two lenses are 5.16 mm and 3.10 mm, respectively. Both lenses are AR-coated. Intensity on target is about 2.1 GW/m<sup>2</sup> when 15 W peak are incident from the 4 lasers.

A small stepper motor drives the closed-loop fuel tape in the longitudinal direction at speeds of 5 to 20 mm/s. A second stepper motor slowly advances the beam delivery system (fiber ends and two lenses) across the tape at a rate of one track width per revolution of

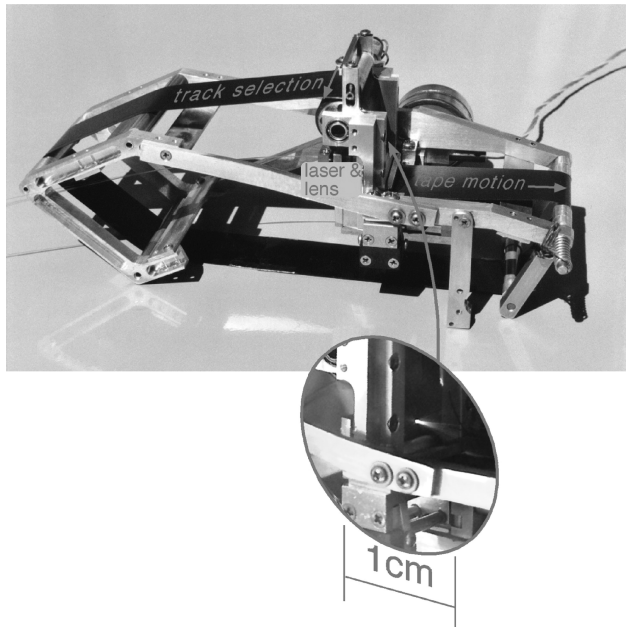


Fig. 3 Testbed microthruster.

the tape loop, resulting in a continuous helical path that eventually accesses the entire tape and produces uniformly spaced burn spots.

We always operated the  $\mu$ LPT testbed in repetitively-pulsed mode, because we found that the moving tape steers the  $\mu$ LPT jet unacceptably in CW mode. During a ms-duration pulse, however, tape motion is negligible and the plume is well-defined and perpendicular to the tape. This change brought with it three benefits: operation in closer contact with the bulk of our test data (which is impulse data), operation at higher peak power for better  $I_{sp}$ , and low duty factor operation of our laser diodes, which is better for their heat dissipation.

Pulse width, pulse repetition frequency, speed for both motors, total running time, laser current and rate of change of motor speed are controlled by an onboard Texas Instruments, Inc. MSP430 microcontroller which consumes only 7 mW at full computing speed and 5  $\mu$ W at standby. An asynchronous optical transmit/receive link transmits commands to, and data from the unit when it is under vacuum. Commands are formatted and data interpreted by an external control console with a National Instruments, Inc. Labview<sup>TM</sup> graphical user interface.

Power is supplied to the testbed thruster by onboard Li-ion batteries to eliminate any external torsion inputs.

A third motor and detector pair allows the operator to control the beam delivery system focus adjustment from outside the vacuum chamber.

For the testbed  $\mu$ LPT (Table 3)  $k \sim 600$ . For our commercial microthruster now under construction, which differs only in its (smaller) physical size and in the amount of ablation fuel on board [Table 4],  $k \sim 4$ . In both devices, dry mass includes the electronics boards' mass.

### Ablation Tape Design

Ablation fuel tapes were made by the use of a variety of substrates and ablative coatings. Substrates were chosen for transparency, resistance to solvents and moisture, toughness, low outgassing, and high optical damage resistance. We found that these requirements tended to be mutually exclusive: For example, Kapton<sup>TM</sup> polyimide resin has excellent toughness and outgassing properties, but lower optical damage resistance compared to cellulose acetate (Table 5). Of the materials listed, only cellulose acetate and FEP Teflon<sup>TM</sup> were excellent in regard to optical damage resistance. Because FEP had the added problem of poor adhesion to coatings other than vapor-deposited aluminum (the problem responsible for the marginal evaluation under mechanical properties), we were left with cellulose acetate as the best performing substrate for general use and polyimide as the selection for the designed photopolymer coatings, where the application process involves solvents not tolerated by the cellulose

Table 3 Parameters for the testbed  $\mu$ LPT (test unit, this paper)

| Parameter                                      | Value  |
|--|--|
| Weight with fuel                               | 0.75 kg  |
| Expendable fuel mass                           | 1.3E-3 kg                                      |
| $k$ value                                      | 585  |
| Tape dimensions                                | 0.505 m $\times$ 0.0254 m $\times$ 160 $\mu$ m |
| Laser wavelength                               | 920 nm   |
| Peak laser power <sup>a</sup>                  | 15 W   |
| Average laser power                            | 2.4 W  |
| Laser focal spot diameter                      | 170 $\mu$ m                                    |
| Laser spot scanning speed                      | 0.020 m/s                                      |
| Pulse duration $\tau$                          | 2 ms   |
| Pulse repetition frequency                     | 80 Hz  |
| Track width, normal operation                  | 100 $\mu$ m                                    |
| Tape lifetime                                  | 1.8 h  |
| Coupling coefficient                           | 400 $\mu$ N/W                                  |
| Incident laser intensity on target $\phi/\tau$ | 660 MW/m <sup>2</sup>                          |
| Force output                                   | 960 $\mu$ N                                    |
| Lifetime impulse                               | 6.2 N · s                                      |
| $Q^*$  | 12 MJ/kg                                       |
| $I_{sp}$                                       | 400 s  |
| Minimum impulse bit                            | 1 $\mu$ N · s <sup>b</sup>                     |

<sup>a</sup>With fiber-coupled diode lasers. <sup>b</sup>At 1-ms pulse width.

acetate. Tape substrate thickness ranged from 75 to 125  $\mu\text{m}$ . Coatings ranged from 60 to 370  $\mu\text{m}$ .

Passive (nonexothermic) ablative coatings for tapes were applied as a spray, in increments of 5  $\mu\text{m}$ , to attain an ideal total thickness of order 70  $\mu\text{m}$ . Exothermic ablative coatings were applied in a single application via a draw-blade applicator.

#### Photopolymer Carbon Selection

In the creation of all target polymers, carbon was added as a laser absorber. Carbon can be applied in various forms, all of which exhibit slightly different properties. Therefore, various carbons were tested as dopants for polymers in  $\mu\text{LPT}$  experiments. For these experiments, four different types of carbon were selected (basic, acidic, and conducting carbon soot, plus carbon nanopearls with a nominal particle size of 5–10 nm). A standard polymer was used (Alcotex<sup>TM</sup> = polyvinyl alcohol/polyethylene glycol copolymer) as matrix because the exothermic polymers are more difficult to prepare. Samples were prepared, and the momentum coupling coefficient and specific impulse were measured. The best performance was obtained for the carbon nanopearls, which will be used for all future work.

#### Photopolymer Preparation

For the carbon-doped triazene-polymer films, chlorobenzene was used as the solvent; for the carbon-doped polyvinyl alcohol (PVAlc, Alcotex<sup>TM</sup>, Hoechst) a water/methanol mixture was used, whereas for the polybutadiene, hexane was used as solvent. The polymer solutions were combined with carbon suspensions (prepared with a high-speed stirrer, Ultra-Turrax T25, in the same solvent as the polymer) and mixed with the high-speed stirrer. The films ( $\geq 60 \mu\text{m}$ ) were prepared by drawing (draw-blade applicator, Industry Tech) the suspensions onto polymer substrates (PET and PI). The decomposition temperature and enthalpy of the polymers were measured with a differential scanning calorimeter (DSC) (Perkin–Elmer DSC 7) under  $\text{N}_2$  with heating rates from 10–20  $\text{K min}^{-1}$ .

The proprietary EP-1 was also doped with carbon, followed by several processing steps for example, crosslinking, to prepare the films.

**Table 4 Parameters for the commercial prototype  $\mu\text{LPT}$  (under construction)**

| Parameter                                      | Value   |
|--|---|
| Weight with fuel                               | 0.52 kg   |
| Expendable fuel mass                           | 0.1 kg  |
| $k$ value                                      | 4.2   |
| Tape dimensions                                | 39.4 m $\times$ 0.0254 m $\times$ 160 $\mu\text{m}$ |
| Laser wavelength                               | 920 nm  |
| Peak laser power <sup>a</sup>                  | 15 W  |
| Average laser power                            | 2.4 W   |
| Laser focal spot diameter                      | 170 $\mu\text{m}$                                   |
| Laser spot scanning speed                      | 0.02 m/s  |
| Pulse duration $\tau$                          | 2 ms  |
| Pulse repetition frequency                     | 80 Hz   |
| Track width, normal operation                  | 100 $\mu\text{m}$                                   |
| Tape lifetime                                  | 140 h   |
| Coupling coefficient                           | 400 $\mu\text{N/W}$                                 |
| Incident laser intensity on target $\phi/\tau$ | 660 MW/ $\text{m}^2$                                |
| Force output                                   | 960 $\mu\text{N}$                                   |
| Lifetime impulse                               | 484 N · s   |
| $Q^*$  | 12 MJ/kg  |
| $I_{\text{sp}}$                                | 400 s   |
| Minimum impulse bit                            | 1 $\mu\text{N} \cdot \text{s}$ <sup>b</sup>         |

<sup>a</sup>With fiber-coupled diode lasers. <sup>b</sup>At 1-ms pulse width.

#### Measurement Methods

Two measurement setups were employed.

##### Impulse Test Stand

Millimeter-size samples of candidate target materials were evaluated with the highly sensitive torsion balance described earlier.<sup>3</sup> With this device, impulse from millisecond-duration single shots of a diffraction-limited 935-nm diode laser (JDSU Model XC-30), focused to 5- $\mu\text{m}$  FWHM, was measured to give  $C_m$  vs pulse energy. Because the amount of material removed was in the nanogram range, it was impossible to measure mass loss directly, and so  $I_{\text{sp}}$  was deduced from the size of the crater produced in the target by the use of a measuring microscope. Although throughput of the vacuum system attached to this test chamber was limited, single shots did not raise the base pressure significantly from about  $9E-5$  torr.

##### Thrust Test Stand

In the second setup, force rather than impulse was measured. In this setup, the entire thruster and its electronics were suspended by a much larger torsion balance in vacuum, rotation of the balance being proportional to the thrust (Fig. 4). To obtain data in seconds rather than minutes, because the settling time of the large-torsion pendulum was several minutes, we also used a flag pendulum mounted very close to the jet. Although the sticking fraction of plume components to the flag could not be measured, agreement between the two thrust measurement techniques was good.

Performance of these two gauges is summarized in Table 6. The repeatability of thrust measured by the torsion thrust stand was improved to 1  $\mu\text{N}$  when the power delivery method was changed to onboard batteries.

After initial thrust measurements in a different chamber, similar to the one used for impulse measurements, an unacceptable base pressure in the millitorr range resulted. The setup was moved to a high throughput chamber that achieved a several microtorr base pressure in the presence of the microthruster exhaust loading.

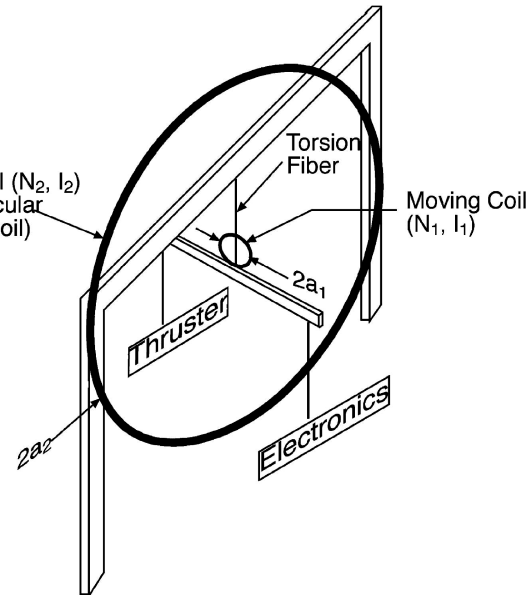


**Fig. 4 Magnetic torque calibration of torsion thrust stand.**

**Table 5 Comparison of tape substrate properties**

| Material          | Optical transmission | Chemical  | Mechanical | Outgassing | Damage resistance |
|-------------------|----------------------|-----------|------------|------------|-------------------|
| Cellulose acetate | Excellent            | Poor      | Marginal   | Adequate   | Excellent         |
| Polyimide         | Adequate             | Excellent | Excellent  | Excellent  | Marginal          |
| PET               | Excellent            | Adequate  | Adequate   | Adequate   | Marginal          |
| FEP               | Marginal             | Excellent | Marginal   | Excellent  | Excellent         |

**Table 6 Comparison of thrust measurement methods employed**

| Data type | Pendulum             | Quantity measured | Mass capacity | Response                                    | Resolution                       | Capacity                       |
|-----------|----------------------|-------------------|---------------|---|----------------------------------|--------------------------------|
| Impulse   | Small torsion        | Impulse           | $2E-5$ kg     | $6.8 \mu\text{N} \cdot \text{s}/\text{rad}$ | $1E-10 \text{ N} \cdot \text{s}$ | $3 \mu\text{N} \cdot \text{s}$ |
| Thrust    | Torsion thrust stand | Thrust            | 17 kg         | $5.0 \text{ mN}/\text{rad}$                 | $20 \mu\text{N}$                 | $3 \text{ mN}$                 |
| Thrust    | Flag pendulum        | Thrust            | $3.75E-4$ kg  | $3.4 \text{ mN}/\text{rad}$                 | $20 \mu\text{N}$                 | $1.5 \text{ mN}$               |

### Calibration

All three thrust measurement devices were calibrated from first principles. The impulse measurement torsion device was calibrated with an applied force applied by a simple pendulum.<sup>3</sup> The large torsion device was calibrated with an even more basic source, namely, magnetic torque between a fixed and a moving Helmholtz coil.

The response of the flag pendulum was calculated from the measured mass of its components and their spacial distribution. This is a primary calibration because no material properties (such as spring constants) are involved in the operation of the flag pendulum.

For the two coils, with  $a_2 = 0.219 \text{ m} \gg a_1 = 0.039 \text{ m}$  (Fig. 4), the torque  $T$  is

$$T = mB = \frac{\mu_0 \pi a_1^2}{2a_2} i_1 i_2 N_1 N_2 \quad N - m \quad (22)$$

We had  $N_1 = 20$  and  $N_2 = 300$ . We measured the pendulum rotation vs combinations of  $i_1$  and  $i_2$  to determine

$$T = 774 \mu\text{N} \cdot \text{m}/\text{rad} \pm 10\% \quad (23)$$

The length of the arm from the torsion fiber to the jet centerline  $R_1 = 0.0155 \text{ m}$ , so that

$$F/\theta = 5 \text{ mN}/\text{rad} \pm 10\% \quad (24)$$

which is the calibration value to which we refer in Table 6.

### Cavity Volume and Impulsive $I_{sp}$

Microscopic measurement of laser-produced cavity size was accomplished when the excavated volume was modeled as a truncated cone, with major and minor diameters  $a_1$  and  $b_1$  and  $a_2$ , and  $b_2$  at the top and bottom, respectively, and depth  $h$ . The bottom of the hole is at the interface with the transparent substrate.

Then

$$\Delta m = \rho(\pi h/12)[a_1 b_1 + a_2 b_2 + (a_1 b_1 a_2 b_2)^{0.5}] \quad (25)$$

The truncated cone assumption matches the holes for which we took data well because holes that did not match this shape were not measured.

### Intercepted Mass Fraction

The testbed design suffers from having several components located forward of the jet and very slightly off axis on one side. These components absorb a portion of the exhaust and, therefore, reduce the measured thrust. We quantified this problem by installing a very light metal foil that completely covered those portions of the apparatus, then carefully measured the mass gain of the foil and compared that quantity with the total mass loss from the fuel tape. This measurement was repeated several times to reduce scatter and ultimately determine that the jet interception is a  $20 \pm 2\%$  effect in our measurements.

The effects on data are as follows.

First, because measured thrust is reduced by 20% relative to the true value, measured thrust and measured thrust  $C_m$  are corrected upward by a factor of 1.20 in the data reported here.

Second, because  $I_{sp}$  is determined from the product  $C_m Q^*$  [Eq. (2)], thrust  $I_{sp}$  values reported here also include this 1.20 factor.

### Error Analysis

#### Laser Pulse Parameters

Pulse duration and repetition frequency for the lasers used in both impulsive and thrust measurements were carefully calibrated with a highly accurate detector and oscilloscope combination and are accurate to within  $\pm 2\%$ . The pulse generator for the XC-30 used in the impulse measurements was factory calibrated to  $\pm 1\%$  accuracy. Pulse current amplitude driving the thrust lasers was measured to within  $\pm 5\%$  accuracy by the use of a current viewing resistor and the oscilloscope. The relationship between optical power and driving current for each laser type is also a JDS Uniphase Corporation (JDSU) factory calibration, accurate to within  $\pm 2\%$ . As a result, we could set pulse duration and pulse current amplitude and predict laser optical pulse energy in either setup to within  $\pm 7\%$ . However, time-average optical output power was separately related to time-average electrical input power by the use of a Scientech power meter, and agreement with the pulse energy measurements was within  $\pm 5\%$ . Accordingly, we claim laser pulse energy is accurate to within  $\pm 5\%$ .

#### Impulse $I_{sp}$

Craters made with the impulse test stand setup were individually measured under 20–100-times magnification and their dimensions determined with an accuracy of  $\pm 5\%$ . However, we take the error estimate on  $\Delta m$  to be  $\pm 30\%$  and  $I_{sp}$  measured with the impulse test stand to be  $\pm 50\%$ , larger than that which would be deduced from dimensional inaccuracy alone. This value is an estimate and includes effects that we cannot directly measure in any other way, including the extent to which the actual hole shape differs from that of a truncated cone, and the extent to which hot outgassing from the material releases vapor that does not correspond to any visible cavity.

#### Impulse $C_m$

There are three quantitative factors contributing to the uncertainty in measuring  $C_m$  with the impulse test setup. The first of these is uncertainty in measuring laser pulse energy  $W$ , which we take as  $\pm 5\%$  as discussed. Uncertainty in the measurement of the gauge deflection was  $\pm 10\%$ , and that of the measurement of its oscillation frequency (inversely proportional to the gauge responsivity) was  $\pm 5\%$ . We take these effects together to develop a  $\pm 20\%$  error bar on impulse test setup  $C_m$  data.

#### Thrust $C_m$

Electrical power for the thruster mounted on the gauge was fed through a cup of liquid mercury, which was invariably covered with a thin film of oxide after any appreciable exposure to air. This film added an unpredictable friction or stiction component to the gauge response. Error in calibration currents measurement was 1%. The majority of error in the torque calibration derived from scatter in the response of the torsion pendulum. Data from the magnetic calibration runs (where the applied force was known and fixed) indicated that a  $\pm 20\%$  error bar for thrust  $C_m$  data is appropriate.

#### Thrust $I_{sp}$

As indicated by Eq. (2), we determine  $I_{sp}$  from the product of  $C_m$  and  $Q^*$ . Uncertainty in  $Q^*$  arises almost entirely from uncertainty in the true mass loss because here, as in the impulse tests, the laser input is relatively accurately known. This, in turn, derives not from our ability to measure mass, which is done quite accurately on a microgram Mettler balance, but from the mass loss that occurs due

**Table 7 Comparison of ablative coating performance**

| Exothermic materials        | Impulse $C_m$ , $\mu\text{N}/\text{W}$ | Impulse $I_{sp}$ , s | $\eta_{ab}$ , % | Thrust $C_m$ , $\mu\text{N}/\text{W}^a$ | Thrust $I_{sp}$ , s <sup>a</sup> | $\eta_{ab}$ , % |
|-----------------------------|--|----------------------|-----------------|---|----------------------------------|-----------------|
| C:EP-1                      | 1170                                   | 540                  | 310             | 640                                     | 430                              | 130             |
| C:Triazene polymer          | 70                                     | 380                  | 13              | —                                       | —                                | —               |
| C:Polyvinyl alcohol         | 10                                     | 40                   | 0.2             | —                                       | —                                | —               |
| C:Nitrocellulose            | 110                                    | 71                   | 3.8             | 150                                     | 97                               | 71              |
| Passive material comparison |  |                      |                 |   |                                  |                 |
| C:PVC                       | 120 <sup>1</sup>                       | 650                  | 38              | 230                                     | 370                              | 42              |

<sup>a</sup>Includes factor of 1.2 upward correction to account for the measured ablation jet fraction absorbed by the apparatus.

to normal outgassing of the tape during the 30 min or so that the tape spends under vacuum in addition to the few minutes of laser irradiation. We believe this effect gives an overall uncertainty of  $\pm 30\%$  to  $Q^*$  and, thus,  $\pm 50\%$  to  $I_{sp}$ .

#### Dimensions $d_x$ , $d_y$ , and $z$

For the varying intensity fixed threshold data, our  $z$  data are accurate  $\pm 10 \mu\text{m}$ , being derived from a dial indicator with that performance. FWHM's deduced at each  $z$  slice are accurate to within  $\pm 10\%$ . Intensity on target is accurate to  $\pm 2\%$ . Data for dimensions  $d_x$  and  $d_y$  are also accurate to within  $\pm 10 \mu\text{m}$ .

## Experimental Results

### Incident Laser Beam Waist Size

To determine incident laser beam fluence, the beam waist diameter at the target must be known. However, because of the power density, no detector could survive at the laser focus, and there is no room for an optical attenuator in the collimated portion of the beam between the collimating and focusing lenses. Standard commercial instruments are not suitable for the measurement.

Instead, we determined the incident laser beam shape  $I(r, z)$  approaching focus using the self-calibrating "varying intensity, fixed threshold" (VIFT) technique,<sup>27–29</sup> and used these data to accurately determine  $2w_0$ . In this technique, a sharp-burn-threshold film was placed at eight different positions  $z$  from best focus to  $500 \mu\text{m}$  away from best focus. In our case, this was an 18- $\mu\text{m}$  coating of C:PVC on cellulose acetate. Then, the film was subjected to a series of pulses of constant duration but increasing incident laser power ranging from 1 to 13.5 W, and the size of the burn spots in both dimensions were recorded. Given a fixed damage threshold, this establishes beam shape for that  $z$  slice through the beam. The process was repeated at several positions to determine  $I(r, z)/I_0$ . Because the lowest-power point will only accidentally coincide with target damage threshold, the trend must be extended to zero diameter to determine damage threshold intensity for the target. 2.718 times intensity is that value that gives the diameter of the beam at a particular  $z$  (Fig. 5).

The  $z$  dependence in  $I(r, z)$  is given by<sup>30</sup>

$$[w^2(z) - w_0^2] = [(\lambda_{\text{eff}}/\pi w_0)(z - z_0)]^2 \quad (26)$$

where  $w$  is beam radius,  $z$  is axial position,  $w_0$  is the minimum radius (beam waist) at best focus ( $z_0$ ),  $\lambda_{\text{eff}} = M^2\lambda$  and  $M^2$  is the beam quality factor normally expressed as  $M^2$  times diffraction limited. Each data spot diameter is determined as  $d = (d_x * d_y)^{0.5}$ , where  $d_x$  and  $d_y$  are the measured vertical and horizontal burn spot dimensions. The reference plane for all measurements is the interface between the substrate and the PVC coating.

After the entire series of results is fit (Fig. 6), a value for  $\text{FWHM}(z = z_0)$  can be deduced that is more accurate than that determined at a single value of  $z$ . We conclude that  $2w_0 = 170 \pm 10 \mu\text{m}$  and the beam quality factor  $M^2 = 95$ .

### Performance of the Exothermic Coatings

Table 7 lists the performance of exothermic coatings that we tried. In Fig. 7 the momentum coupling coefficients measured with the impulse test stand at various laser fluences of the carbon-doped triazene polymer and of a carbon-doped PVAlc are shown. The triazene

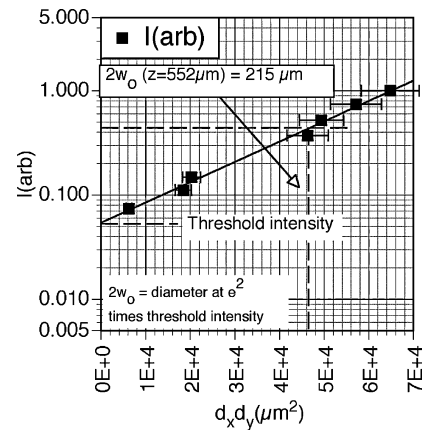


**Fig. 5 Series of exposures at each axial position  $z$ , allowing determination of beam diameter  $d = (d_x d_y)$  at that position. Threshold intensity is obtained by extrapolating to zero diameter, using a Gaussian radial intensity distribution  $I(r, z)/I_0 = \exp(-2r^2/w^2)$ . Such a fit gives the straight line shown on a semilog plot. The existence of this particular slice through the irradiance distribution is that, at  $z = 552 \mu\text{m}$ , the beam waist diameter is  $2w_0 = 215 \mu\text{m}$ .**

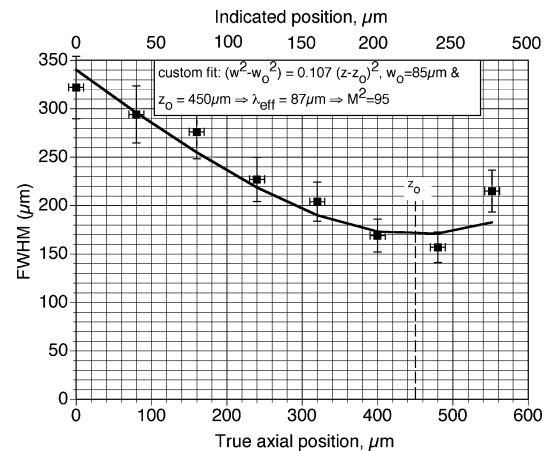


**Fig. 6 Beam diameter vs position  $z$  near focus, determined by the VIFT technique illustrated in Fig. 5; the point from Fig. 5 is the rightmost one with this figure.**

polymer reveals higher coupling coefficients and, more importantly, quite a well-defined threshold for a maximum  $C_m$ . In Fig. 8 the specific impulse  $I_{sp}$  at various laser fluences are shown. The carbon-doped triazene polymer clearly reveals a higher specific impulse than the polyvinyl alcohol. The fewer data points for the triazene polymer are due to the very irregular shape of the craters that did not allow measurements of the ablated volume at all laser fluences. The  $I_{sp}$  values are clearly higher for the triazene polymer and probably reveal a threshold at a similar fluence range as for  $C_m$ .

The well-defined threshold and higher  $C_m$  of the triazene polymer is an important feature for the design of a plasma thruster with

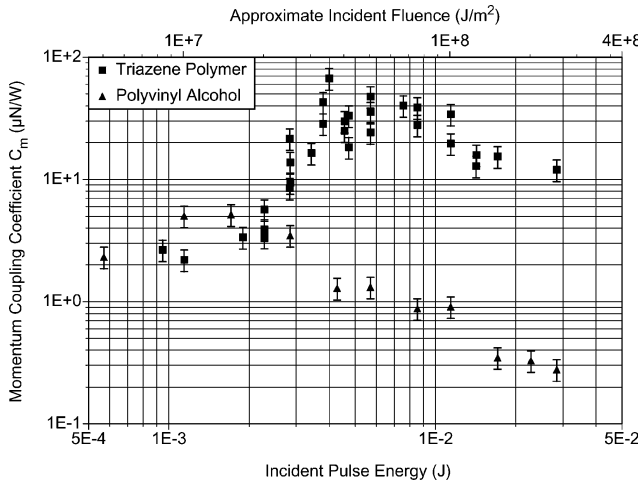


**Fig. 7** Momentum coupling coefficients  $C_m$  at various fluences for the carbon-doped exothermic photopolymers. Optical density at 935 nm  $\approx 0.9$ , film thickness  $\approx 65 \mu\text{m}$ , PET substrates (impulse test stand).

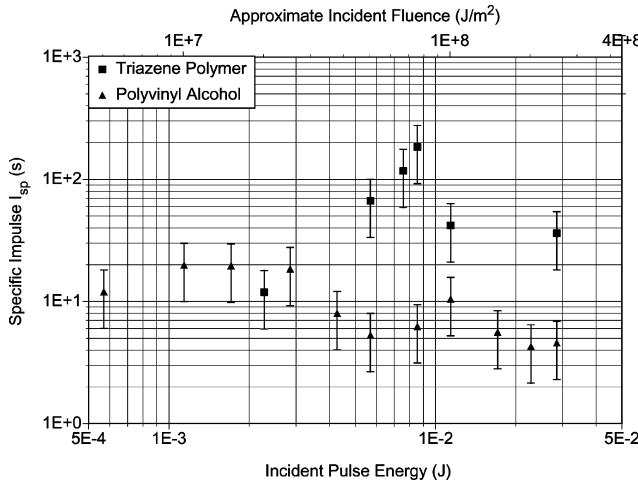


**Fig. 8** Specific impulse at various fluences for the carbon-doped exothermic polymers. Same materials as in Fig. 5 (impulse test stand).

tapelike polymer fuel because the optimum incident laser fluence and tape speed are clearly defined. The decreasing values of  $C_m$  after the maximum are due to the increasing fraction of incident laser energy devoted to accelerating vapor, then to creating plasma and to absorption of the laser energy by the created plasma.<sup>19</sup> The well-defined threshold and higher values are probably due to the decomposition properties of the triazene polymer. The thermal decomposition, initiated by absorption of the laser energy by the carbon, most probably follows the same pathway as the UV laser-induced decomposition. The  $N_3$  group is the photolabile group in the polymer, but also the primary decomposition site of thermolysis, as suggested by product analysis by mass spectrometry.<sup>31</sup> In thermolysis, the triazene polymer exhibits a well-defined, quite sharp ( $\text{FWHM} \approx 60^\circ\text{C}$ ) decomposition temperature ( $\approx 227^\circ\text{C}$ ) and an exothermic decomposition enthalpy ( $\approx -0.7 \text{ MJ} \cdot \text{kg}^{-1}$ ), whereas the PVAlc exhibit a very broad ( $\text{FWHM} \approx 200^\circ\text{C}$ ) decomposition peak centered around  $260^\circ\text{C}$ . The decomposition is also exothermic ( $< -0.5 \text{ MJ} \cdot \text{kg}^{-1}$ ), but the enthalpy could not be determined exactly due to the sloping, ill-defined baseline of the DSC scans. Whether the amount of released energy, the maximum temperature, or the width of the decomposition process are more important for creating a threshold for a maximum  $C_m$  is not clear at the moment.

Figure 9 shows the extremely sharp threshold obtained for the proprietary exothermic EP-1 coating. Of the three exothermic coatings, it is the best performer.

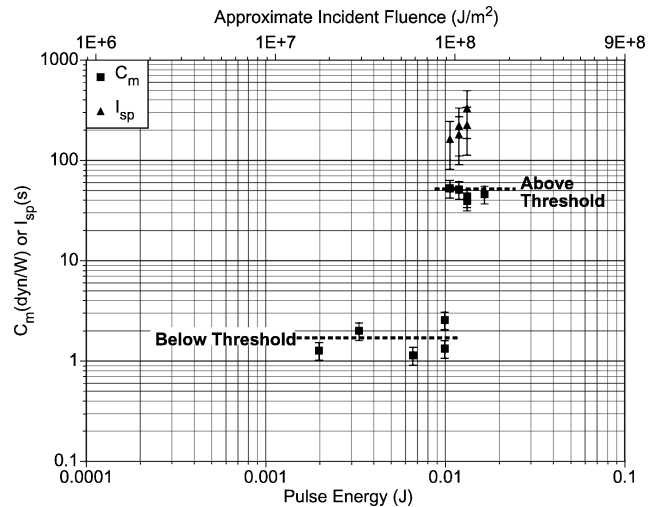


**Fig. 9** Impulse coupling data for EP-1 coating (0.5% carbon nanopearls) shows an even sharper threshold than that in Fig. 8, a factor-of-30 increase in  $C_m$  at  $10 \text{ mJ} \pm 1 \text{ mJ}$  input energy. With a laser illumination diameter of  $170 \mu\text{m}$  ( $1/\text{e}^2$ ), this corresponds to  $440 \text{ kJ/m}^2$  for incident fluence at threshold. Pulselength was varied at constant peak power to obtain variations in pulse energy for these tests. Threshold pulselength was 10 ms, giving  $44 \text{ MW/m}^2$  as the incident intensity at threshold (impulse test stand).

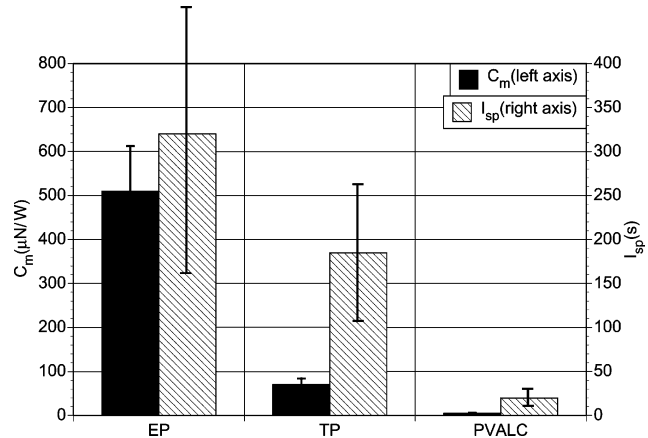


**Fig. 10** Comparison of the maximum  $C_m$  and  $I_{sp}$  for three selected polymers (impulse test stand).

A comparison of the momentum coupling coefficients  $C_m$  and specific impulse  $I_{sp}$  is shown on a logarithmic scale in Fig. 10. Figure 10 shows that  $C_m$  increases by one order of magnitude from PVAlc (Buna is similar) to TP and again to EP-1. The momentum coupling coefficients for EP-1 are among the highest reported values for a polymer coating ( $640 \mu\text{N}/\text{W}$ ). The values of thrust obtained are also in a range such that the TechSat21 thrust specifications are exceeded by an order of magnitude. The specific impulse increases also in the same order, to reach a maximum value for EP-1 of 546 s.

The thermal decomposition of the EP-1 material is more exothermic than for the other polymers tested (about  $-2.1 \text{ MJ/kg}$ ). The main decomposition product is nitrogen, as in the case of TP. The decomposition temperatures are also in a similar range for most polymers (at least for TP and EP-1).

At threshold, the laser is contributing  $6.7 \text{ MJ/kg}$ , and so laser energy contributes 24% to the interaction. At higher incident fluence, the laser contributes a larger proportion.

Figure 11 summarizes our experimental data for  $C_m$  and  $I_{sp}$ , plotted in a format suggested by Eq. (4), together with the hyperbolic plots representing 50 and 100% ablation efficiency for passive targets, which are included as performance references even for the exothermic data. It is seen that several of the impulse data exceed

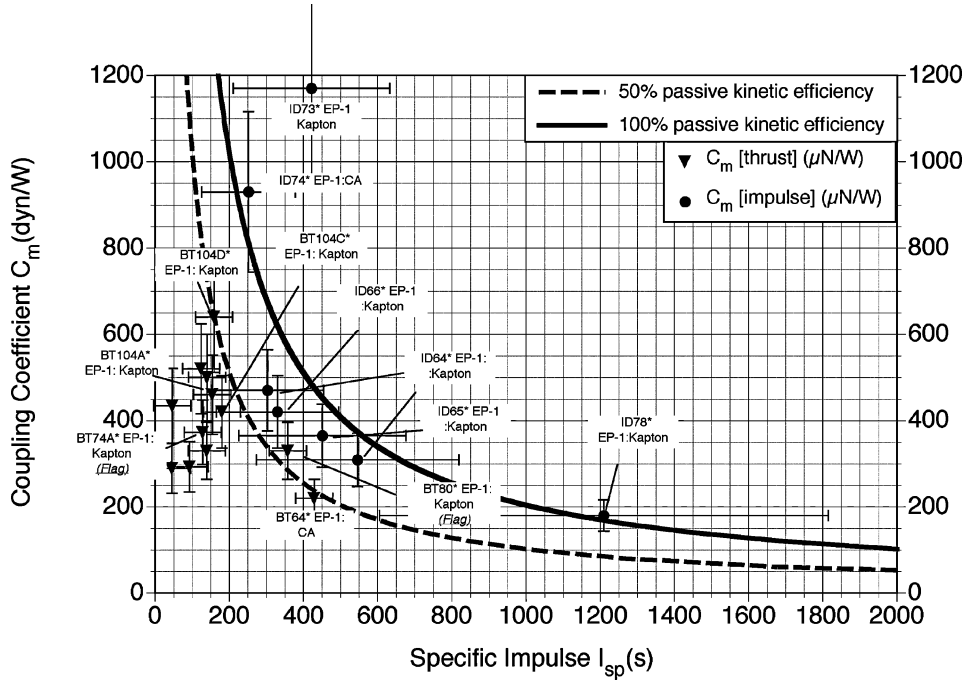


**Fig. 11** Compilation of  $C_m$  and  $I_{sp}$  data on exothermic materials, plotted in a format suggested by Larson et al.<sup>32</sup> data from thrust tests measured with the microthruster mounted on a torsion balance and ●, single-pulse impulse data.

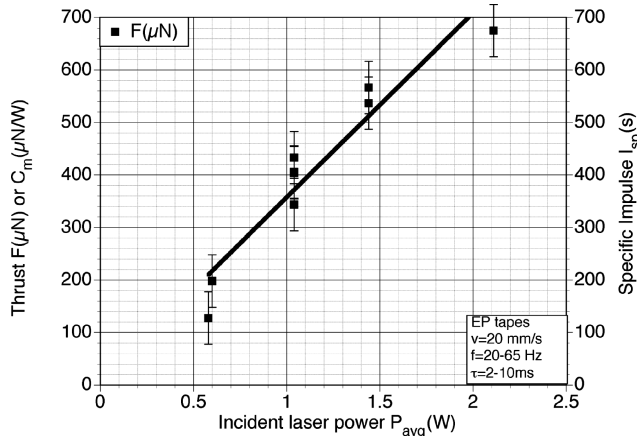


**Fig. 12** Thrust data for tapes using EP-1 absorbing material vs time-average incident laser power; thrust includes factor of 1.2 upward correction to account for the measured ablation jet fraction absorbed by the apparatus.

the 100% efficiency curve, as they should. Thrust stand data cluster around the 50% efficiency curve. Figure 12 shows the thrust performance of the exothermic coatings vs laser power.

#### Discrepancy Between Impulse and Thrust Stand Measurements

Both specific impulse and coupling coefficient are substantially higher in impulse compared to thrust stand measurements, by as much as a factor of two. We have identified several reasons for this discrepancy. Two of these derive from the fact that the impulse test laser is single mode, whereas the thrust stand test laser is multimode and has to be focused more strongly to reach a useful intensity. The factors explaining the discrepancy are as follows.

- 1) The laser spot size in the impulse setup is 12 vs 170  $\mu\text{m}$  in the thrust stand setup. As a result of the larger illumination spot in the thrust stand test setup, despite far higher peak laser power, the intensity (watts per square centimeter) delivered to the target is five times lower, and the target material is not heated to as high a temperature.

2) In the impulse tests, the laser beam can be focused onto the target with a relaxed numerical aperture of 0.2, whereas the thrust stand setup must use a strongly cone-shaped ( $NA = 0.6$ ). As a consequence, in the worst case of a 370- $\mu\text{m}$  coating thickness, the majority of the coating material in the illumination cone sees up to six times less than the peak incident intensity, whereas, for an impulse test of the same coating, the minimum intensity in the volume is only two times less than peak incident intensity.

3) The fact that the particles in the coating are exposed to widely different intensities during illumination in the thrust stand test setup is an especially crucial factor for the  $C_m$  discrepancy, because the exothermic materials have a sharp threshold.

4) A further input to the difference in  $I_{sp}$  in the two cases, which we do not yet have sufficient data to quantify, are the different ways in which  $I_{sp}$  is measured. For the impulse tests, as mentioned earlier, we infer  $\Delta m$  from the size of the cavity produced by the use of a microscope. This ignores the mass of gas that leaks out of the coating after the detonation (hot outgassing), and gives higher than the true value for  $I_{sp}$ . However, this mechanism ought to affect impulse and thrust stand tests equally, especially because we use repetitive pulse operation in the latter.

5) Cold outgassing is an important factor affecting mass loss and, thus,  $I_{sp}$  determination during the 30-min preparation for a thrust stand measurement under vacuum, where the targets are weighed before and after the test to determine  $Q^*$  and then  $I_{sp}$  via Eq. (2).

6) The current preprototype thruster is designed in such a way that the device itself intercepts 20% of the generated thrust. The exhaust is free to expand in the one-half-space away from the forward portion of the fuel tape, but is partially absorbed by apparatus in the other one-half-plane. As a result, measurements reported of  $C_m$  (and, therefore, of  $I_{sp}$ ) are low by a factor of 1.20, and the product  $C_m I_{sp}$ , and consequently  $\eta_{ab}$ , are low by  $(1.20)^2 = 1.44$ . Thrust stand data are shown with and without this correction.

That said, there are probably other reasons for this discrepancy that we do not yet understand.

#### Thermodynamic and Optical Parameters for EP-1 Coating

Figure 13 shows the application of the volume absorber modeling [Eq. (18)] to typical EP-1 data. Note that the interaction area  $A_{ab}$  observed on the target is different from the laser spot area  $A_s$ . The crater is formed by hot vapor and plasma, which mediate the laser

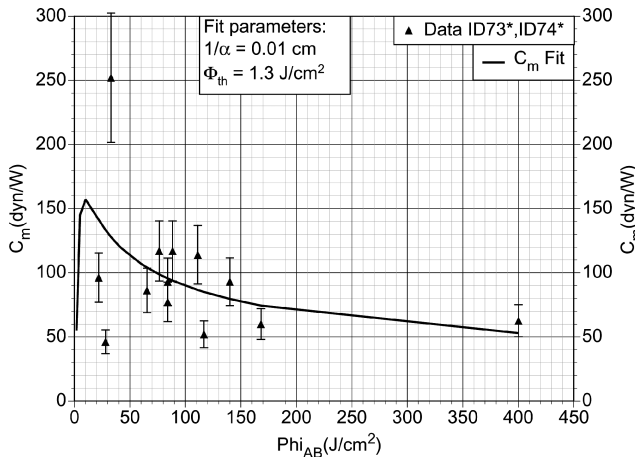


Fig. 13 Best fit to impulse data for proprietary exothermic coating by the use of Eq. (13) gives  $1/\alpha = 100 \mu\text{m}$  and  $\Phi_{th} = 1.3 \text{ J/cm}^2$ ; separate measurements of ablation depth vs fluence by T. Lippert using Eq. (13) gave  $1/\alpha = 50 \mu\text{m}$  and  $\Phi_{th} = 3.1 \text{ J/cm}^2$  (model successfully reproduces the qualitative behavior of the data, especially the sharp rise at very low fluence, but data are shifted horizontally with respect to the model).

energy transfer to the target material and act as the effective source. This idea is sustained by photomicrographs of the crater, which show it to be of more or less uniform depth, lacking a central spike.

Fluence  $\Phi_{ab}$  in the Fig. 13 data plot is determined via the measured crater area  $A_{ab}$  on the target rather than the incident beam area  $A_s$  (Table 1).

Finally, we can deduce a threshold exhaust velocity from Eq. (13) that is consistent with our other measurements. The quantity  $h_c$  was separately measured to be 2053 MJ/kg. From Eq. (17), we then obtain  $v = 2.0 \text{ km/s}$ , or  $I_{sp} = 210 \text{ s}$ , which agrees well with our measurements of  $I_{sp}$  near threshold.

#### Testbed Microthruster Performance

During the thrust measurements reported here, the micro-LPT logged 7.68 h of operation. The device demonstrated a system thrust-to-power ratio  $C_{ms} = 75 \mu\text{N/W}$  relative to total electrical input and a ratio of exhaust power to electrical input of 8%, a ratio sometimes called “thrust efficiency.” These numbers suffer from laser pulse drive circuitry used in the current model which is only 30% efficient.

#### Conclusions

Ablation efficiency  $\eta_{ab}$  increased by a factor of 2–3 in going from C:PVC to EP-1 as an ablative fuel. This was accomplished primarily by an increase of  $C_m$ , though  $I_{sp}$  also increased to some degree. We succeeded in obtaining more than three times as much thrust for the same optical power input [240 vs 75  $\mu\text{N}$  at 0.65 W (Ref. 11)].

We proved theoretically and experimentally that our operating point was far away from explosive, propagating detonations in the fuel.

We have discussed the theory behind the laser–material interaction for a rear-illuminated heterogeneous ablation system that generates very high pressures through a combination of confined ablation (so-called volume absorber mode) and exothermic ablatants.

We reported the performance of deliberately designed exothermic photopolymers that are the basis of an ablation fuel tape for the  $\mu$ LPT, which is able to generate 640- $\mu\text{N}$  thrust per watt of incident optical power. Ablation depth data and coupling data were all consistent with thruster exhaust velocity of 1.2–4.2 km/s, 430 s specific impulse, absorption depth 50–100  $\mu\text{m}$ , and threshold fluence 13–31 kJ/m<sup>2</sup> for the proprietary carbon-doped exothermic absorber.

#### Acknowledgments

This work was supported by the U.S. Air Force under contracts F04611-02-M-0025, F49620-00-C-0005, F49620-980C-0038, and by the Swiss National Science Foundation. It is also based in part on

work supported by the European Office of Aerospace Research and Development, U.S. Air Force Office of Scientific Research, U.S. Air Force Laboratory, under Contract F61775-01-WE057.

#### References

- <sup>1</sup>Phipps, C. R., and Luke, J. R., “Diode Laser-Driven Microthrusters: A New Departure for Micropulsion,” *AIAA Journal*, Vol. 40, No. 2, 2002, pp. 310–318.
- <sup>2</sup>Leach, R., “Development of Hardware for a Drag-Free Control System,” *Proceedings of the SPIE Astronomical Telescopes and Instrumentation Conference*, Society of Photo-Optical Instrumentation Engineers, Bellingham, WA, 2002.
- <sup>3</sup>Mueller, J., “Thruster Options for Microspacecraft: A Review and Evaluation of State-of-the-Art and Emerging Technologies,” *Micropropulsion for Small Spacecraft*, Vol. 187, Progress in Astronautics and Aeronautics, edited by M. Micci and A. Ketsdever, AIAA, Reston, VA, 2000, Chap. 3.
- <sup>4</sup>Mueller, J., Marrese, C., Ziemer, J., Green, A., Yang, E. H., Mojarradi, M., Johnson, M. T., White, V., Bame, D., Wirz, R., Tajmar, M., Hruby, V., Gamero-Castaño, M., Schein, J., and Reinicke, R., “JPL Micro-Thrust Propulsion Activities,” *AIAA Paper 2002-5714*, Sept. 2002.
- <sup>5</sup>Phipps, R., and Luke, J. R., “A Diode-Laser-Driven Microthruster,” International Electric Propulsion Conf., Paper IEPC-01-220, Oct. 2001.
- <sup>6</sup>Keidar, M., Boyd, I. D., Luke, J., and Phipps, C., “Plasma Generation and Plume Expansion for a Transmission-Mode Micro-Laser Ablation Plasma Thruster,” *Journal of Applied Physics*, Vol. 96, No. 1, 2004, pp. 49–56.
- <sup>7</sup>Phipps, C. R., Luke, J. R., and Lippert, T., “Laser Ablation Powered Mini-Thruster,” *Proceedings of High Power Laser Ablation IV*, Society of Photo-Optical Instrumentation Engineers, Vol. 4760, 2002, pp. 833–842.
- <sup>8</sup>Phipps, C. R., Luke, J. R., McDuff, G. G., and Lippert, T., “Diode-Laser-Driven Micropropulsion Engine,” Association Aeronautique et Astronautique de France, AAAF, May 2002.
- <sup>9</sup>Phipps, C. R., Luke, J. R., and Lippert, T., “A Laser-Ablation-Based Micro-Rocket,” *AIAA Paper 2002-2152*, May 2002.
- <sup>10</sup>Lippert, T., David, C., Hauer, M., Nuyken, O., Phipps, C., Robert, J., and Wokaun, A., “Polymers for UV and Near-IR Irradiation,” *Proceedings of the 4th International Symposium on Photoreaction Control and Photofunctional Materials*, Tsukuba, Japan, March 2001.
- <sup>11</sup>Phipps, C. R., Luke, J. R., and McDuff, G. G., “Laser Plasma Thrusters for Small Satellites,” Progress Rept. 2, Contract F49620-00-C-0005, Defense Technical Information Center, Fort Belvoir, VA, Aug. 2001.
- <sup>12</sup>Phipps, C., Luke, J., McDuff, G., and Lippert, T., “Laser Ablation Powered Mini-Thruster,” *Applied Physics A*, Vol. 77, May 2003, pp. 193–201.
- <sup>13</sup>Phipps, C., Reilly, J., and Campbell, J., “Optimum Parameters for Laser-Launching Objects into Low Earth Orbit,” *Journal of Laser and Particle Beams*, Vol. 18, No. 4, 2000, pp. 661–695.
- <sup>14</sup>Phipps, C., and Michaelis, M., “Laser Impulse Space Propulsion,” *Journal of Laser and Particle Beams*, Vol. 12, No. 1, 1994, pp. 23–54.
- <sup>15</sup>Weast, R. (ed.), *CRC Handbook of Chemistry and Physics*, Chemical Rubber Publishing, Cleveland, OH 1978, p. D-71.
- <sup>16</sup>Johnson, R. D., and Holbrow, C. (eds.), *Space Settlements, a Design Study*, NASA Rept. SP-413, 1977.
- <sup>17</sup>Koppel, C., “Electric Propulsion Subsystem Comparisons,” International Astronautical Congress, IAF Paper 99-A.1.08, Oct. 1999.
- <sup>18</sup>Möckel, W., “Optimum Exhaust Velocity for Laser-Driven Rockets,” *Journal of Spacecraft and Rockets*, Vol. 12, No. 1, 1975, pp. 700, 701.
- <sup>19</sup>Phipps, C., Harrison, R., Shimada, T., York, G., Turner, T., Corlis, X., Steele, H., Haynes, L., and King, T., “Enhanced Vacuum Laser-Impulse Coupling by Volume Absorption at Infrared Wavelengths,” *Laser and Particle Beams*, Vol. 8, Nos. 1–2, 1990, p. 281.
- <sup>20</sup>Srinivasan, R., Braren, B., Dreyfus, R., Hadel, L., and Seeger, D., *Journal of the Optical Society of America*, Vol. B3, No. 5, 1986, p. 785.
- <sup>21</sup>Fabbro, R., Fournier, J., Ballard, P., Devaux, D., and Virmont, J., “Physical Study of Laser-Produced Plasma in Confined Geometry,” *Journal of Applied Physics*, Vol. 68, No. 2, 1990, pp. 775–784.
- <sup>22</sup>Sutcliffe, E., and Srinivasan, R., *Journal of Applied Physics*, Vol. 60, No. 9, 1986, p. 3315.
- <sup>23</sup>Yeh, J., *Journal of Vacuum Science and Technology*, Vol. A4, No. 3, 1986, p. 653.
- <sup>24</sup>Pirri, A., “Theory for Momentum Transfer to a Surface with a High-Power Laser,” *Physics of Fluids*, Vol. 16, No. 9, 1973, pp. 1435–1440.
- <sup>25</sup>Pirri, A., Root, R., and Wu, P., “Plasma Energy Transfer to Metal Surfaces Irradiated by Pulsed Lasers,” *AIAA Journal*, Vol. 16, No. 12, 1978, pp. 1296–1304.
- <sup>26</sup>Raizer, Yu., *Laser-Induced Discharge Phenomena*, Consultants Bureau, New York, 1977, pp. 198–249.
- <sup>27</sup>Winer, I., “A Self-Calibrating Technique Measuring Laser Beam Intensity Distributions,” *Applied Optics*, Vol. 5, No. 9, 1966, pp. 1437–1439.

<sup>28</sup>O'Neil, R., et al., "Beam Diagnostics for High Energy Pulsed CO<sub>2</sub> Lasers," *Applied Optics*, Vol. 13, No. 3, 1974, pp. 314–321.

<sup>29</sup>Marquet, L., "Transmission Diffraction Grating Attenuator for Analysis of High Power Laser Beam Quality," *Applied Optics*, Vol. 10, No. 2, 1971, pp. 960, 961.

<sup>30</sup>Kogelnik, H., and Li, T., "Laser Beams and Resonators," *Applied Optics*, Vol. 5, No. 10, 1996, pp. 1550–1567.

<sup>31</sup>Nuyken, O., Stebani, J., Lippert, T., Wokaun, A., and Stasko, A., *Macromol. Chem. Phys.*, Vol. 196, No. 3, 1995, p. 751.

<sup>32</sup>Larson, C. W., Kalliomaa, W., and Mead, F., AIAA Paper

2002-2206, 2002.

<sup>33</sup>Phipps, C., Seibert, D., II, Royse, R., King, G., and Campbell, J., "Very High Coupling Coefficients at Low Laser Fluence with a Structured Target," *Proceedings of High Power Laser Ablation III*, Society of Photo-Optical Instrumentation Engineers, Vol. 4065, 2000, pp. 931–937.

<sup>34</sup>Yabe, T., Phipps, C., Aoki, K., Yamaguchi, M., Nakagawa, R., Mine, H., Ogata, Y., Baasandash, C., Nakagawa, M., Fujiwara, E., Yoshida, K., Nishiguchi, A., and Kajiwara, I., "Micro-Airplane Propelled by Laser-Driven Exotic Target," *Applied Physics Letters*, Vol. 80, No. 23, 2002, pp. 4318–4320.

# 40-YEAR MEETING PAPER ARCHIVES ONLINE!

Each year, AIAA publishes more than 4000 technical papers presented at AIAA conferences. These papers contain the most recent discoveries in aerospace and related fields. No other organization offers this depth and breadth in the aerospace field.

You now have immediate access to more than 100,000 technical papers online!

Beginning with 1963 and adding about 4,000 papers every year, AIAA's online archive allows you to search for the latest developments in:

- Astrodynamic
- Aerodynamics
- Guidance
- Structures
- Fluids
- Propulsion
- Controls
- Modeling and Simulation
- Flight Mechanics
- and more...

Search and purchase only those papers that fit your needs. Papers are delivered in pdf format. Search by:

- Title
- Keyword
- Author
- AIAA Paper Number
- Conference Title
- Publication Year

[www.aiaa.org/paperstore](http://www.aiaa.org/paperstore)

02-0666

Computing-Based Methodology

Aeroelasticity

EnElHajAli and Z. Feng

riure

Exhibit

AIAA

American Institute of Aeronautics and Astronautics

02-0582